PRIFYSGOL BANGOR / BANGOR UNIVERSITY

PRIFYSGOL BANGOR UNIVERSITY

The impact of sea-level rise on tidal characteristics around Australia

Harker, Alexander; Green, Mattias; Schindelegger, Michael; Wilmes, Sophie-Berenice

Ocean Science

DOI:
10.5194/os-2018-104

Published: 19/02/2019

Publisher's PDF, also known as Version of record

Cyswllt i'r cyhoeddiad / Link to publication

Dyfyniad o'r fersiwn a gyhoeddwyd / Citation for published version (APA):
Harker, A., Green, M., Schindelegger, M., & Wilmes, S-B. (2019). The impact of sea-level rise on tidal characteristics around Australia. *Ocean Science*, *15*(1), 147-159. https://doi.org/10.5194/os-2018-104

Hawliau Cyffredinol / General rights
Copyright and moral rights for the publications made accessible in the public portal are retained by the authors and/or other copyright owners and it is a condition of accessing publications that users recognise and abide by the legal requirements associated with these rights.

- Users may download and print one copy of any publication from the public portal for the purpose of private study or research.
- You may not further distribute the material or use it for any profit-making activity or commercial gain
- You may freely distribute the URL identifying the publication in the public portal ?

Take down policy
If you believe that this document breaches copyright please contact us providing details, and we will remove access to the work immediately and investigate your claim.

11. May. 2021

Ocean Sci., 15, 147–159, 2019
https://doi.org/10.5194/os-15-147-2019
© Author(s) 2019. This work is distributed under
the Creative Commons Attribution 4.0 License.

Ocean Science
Open Access

The impact of sea-level rise on tidal characteristics around Australia

Alexander Harker[1,2], **J. A. Mattias Green**[2], **Michael Schindelegger**[1], **and Sophie-Berenice Wilmes**[2]

[1]Institute of Geodesy and Geoinformation, University of Bonn, Bonn, Germany
[2]School of Ocean Sciences, Bangor University, Menai Bridge, UK

Correspondence: Alexander Harker (harker@igg.uni-bonn.de)

Received: 4 September 2018 – Discussion started: 6 September 2018
Revised: 24 January 2019 – Accepted: 24 January 2019 – Published: 15 February 2019

Abstract. An established tidal model, validated for present-day conditions, is used to investigate the effect of large levels of sea-level rise (SLR) on tidal characteristics around Australasia. SLR is implemented through a uniform depth increase across the model domain, with a comparison between the implementation of coastal defences or allowing low-lying land to flood. The complex spatial response of the semi-diurnal M_2 constituent does not appear to be linear with the imposed SLR. The most predominant features of this response are the generation of new amphidromic systems within the Gulf of Carpentaria and large-amplitude changes in the Arafura Sea, to the north of Australia, and within embayments along Australia's north-west coast. Dissipation from M_2 notably decreases along north-west Australia but is enhanced around New Zealand and the island chains to the north. The diurnal constituent, K_1, is found to decrease in amplitude in the Gulf of Carpentaria when flooding is allowed. Coastal flooding has a profound impact on the response of tidal amplitudes to SLR by creating local regions of increased tidal dissipation and altering the coastal topography. Our results also highlight the necessity for regional models to use correct open boundary conditions reflecting the global tidal changes in response to SLR.

1 Introduction

Fluctuations in sea level at both short and long timescales have had, and will have, a significant influence upon societies in proximity of the coast. Coastal areas are attractive locations for human populations to settle for multiple reasons; the land is often flat and well suited for agriculture and urban development, whilst coastal waters can be used for transport and trade, and as a source of food. Being a large island nation, 85 % of the population of Australia (approximately 19.9 million people; ABS, 2016) live within 50 km of the ocean, and the recreation and tourism industries located along the coast are a key part of Australia's economy (Watson, 2011). As such, Australia is particularly sensitive to both short-term fluctuations in sea level (e.g. tidal and meteorological effects) and long-term changes in mean sea level (MSL). Tidal changes in sea level are a major influencing factor on coastal morphology, navigation, and ecology (Allen et al., 1980; Stumpf and Haines, 1998), and the combination of extreme peaks in tidal amplitude (associated with long period lunar cycles; Pugh and Woodworth, 2014) with storm surges (associated with severe weather events) can be a key component of unanticipated extreme water levels (Haigh et al., 2011; Pugh and Woodworth, 2014; Muis et al., 2016). With sea levels around Australia forecast to rise by up to 0.7 m by the end of the century (McInnes et al., 2015; Zhang et al., 2017), understanding how tidal ranges are expected to vary with changing MSL is crucial for determining the potential implications for urban planning and coastal protection strategies in low-lying areas.

As the dynamical response of the oceans to gravitational forcing, tides are sensitive to a variety of parameters, including water depth and coastal topography. Such changes in bathymetry may have an impact on the speed at which the tide propagates and the dissipation of tidal energy, and it may change the resonant properties of an ocean basin. As an extreme example, during the Last Glacial Maximum (when sea level was approximately 120 m lower than in the present day) the tidal amplitude of the M_2 constituent in the North Atlantic was greater by a factor of 2 or more because of amplified tidal resonances there (Egbert et al., 2004; Wilmes and Green, 2014). Consequently, understanding the ocean tides' response to changing sea level has been a subject of recent

research, at both regional (Greenberg et al., 2012; Pelling et al., 2013; Pelling and Green, 2013; Carless et al., 2016) and global scales (Müller et al., 2011; Pickering et al., 2017; Wilmes et al., 2017; Schindelegger et al., 2018).

Current estimates of the global average change in sea level over the last century suggest a rise of between 1.2 and 1.7 mm year^{-1} (Church et al., 2013; Hay et al., 2015; Dangendorf et al., 2017; IPCC, 2013). However, significant interannual and decadal-scale fluctuations have occurred during this period, for example, over the period 1993–2009, global sea-level rise (SLR) has been estimated at 3.2 mm year^{-1} (Church and White, 2011; IPCC, 2013). Studies suggest that global sea level may rise by up to 1 m by the end of the 21st century and by up to 3.5 m by the end of the 22nd century (Vellinga et al., 2009; DeConto and Pollard, 2016). However, sea-level change is neither temporally nor spatially uniform, as a multitude of physical processes contribute to regional variations (Cazenave and Llovel, 2010; Slangen et al., 2012). Part of this signal is attributed to increasing ocean heat content causing thermal expansion of the water column, but most of the rise and acceleration in sea level is due to enhanced mass input from glaciers and ice sheets (Church et al., 2013). The effect of vertical land motion, specifically glacial isostatic adjustment (GIA), should also come under consideration; however, around the Australian coastline, the effect is small (White et al., 2014). Additionally, trends in the amplitude of the M_2 constituent around Australia are as much as 80 % of the magnitude of the trend seen in global MSL (Woodworth, 2010); thus, the impact of changing tides upon regional variations in sea level should not be underestimated.

Here, we expand previous tides and SLR investigations to the shelf seas surrounding Australia, which have received little attention so far despite the north-west Australian Shelf alone being responsible for a large amount of energy dissipation comparable to that of the Yellow Sea or the Patagonian Shelf (Egbert and Ray, 2001). Here, we study the region's tidal response to a uniform SLR signal and consider the impact of coastal defences (inundation of land allowed or coastal flood defences implemented) on the tidal response. Wide areas of this region experience large tides at present, and areas such as the Gulf of Carpentaria are influenced by tidal resonances (Webb, 2012). It is therefore expected that we will see large differences in the tidal signals with even moderate SLR, as it is known that a (near-)resonant tidal basin is highly sensitive to bathymetric changes (e.g. Green, 2010). In what follows, we introduce the Oregon State University Tidal Inversion Software (OTIS), the dedicated tidal modelling software used, and the simulations performed (Sect. 2.1–2.3). To ground our considerations of future tides on a firm observational basis, we conduct extensive comparisons to tide gauge data in Sect. 2.4. Section 3 presents the results, and the paper concludes in the last section with a discussion.

2 Modelling future tides

2.1 Model configuration and control simulation

We use OTIS to simulate the effects of SLR on the tides around Australia. OTIS is a portable, dedicated, numerical shallow water tidal model which has been used extensively for both global and regional modelling of past, present, and future ocean tides (e.g. Egbert et al., 2004; Pelling and Green, 2013; Wilmes and Green, 2014; Green et al., 2017). It is highly accurate both in the open ocean and in coastal regions (Stammer et al., 2014), and it is computationally efficient. The model solves the linearized shallow-water equations (e.g. Hendershott, 1977) given by

$$\frac{\partial \mathbf{U}}{\partial t} + \boldsymbol{f} \times \mathbf{U} = -gH\nabla(\zeta - \zeta_{\mathrm{EQ}} - \zeta_{\mathrm{SAL}}) - \mathbf{F} \tag{1}$$

$$\frac{\partial \zeta}{\partial t} = -\nabla \cdot \mathbf{U}, \tag{2}$$

where $\mathbf{U}$ is the depth integrated volume transport, which is calculated as tidal current velocity $\boldsymbol{u}$ multiplied by water depth H. $\boldsymbol{f}$ is the Coriolis vector, g denotes the gravitational constant, ζ stands for the tidal elevation with respect to the moving seabed, ζ_{SAL} denotes the tidal elevation due to ocean self-attraction and loading (SAL), and ζ_{EQ} is the equilibrium tidal elevation. $\mathbf{F}$ represents energy losses due to bed friction and barotropic–baroclinic conversion at steep topography. The former is represented by the standard quadratic law:

$$\mathbf{F}_B = C_{\mathrm{d}}\boldsymbol{u}|\boldsymbol{u}|, \tag{3}$$

where $C_{\mathrm{d}} = 0.003$ is a non-dimensional drag coefficient, and $\boldsymbol{u}$ is the total velocity vector for all the tidal constituents. The parameterization for internal tide drag, $\mathbf{F}_w = C|\mathbf{U}|$, includes a conversion coefficient C, which is defined as (Zaron and Egbert, 2006; Green and Huber, 2013)

$$C(x, y) = \gamma \frac{(\nabla H)^2 N_{\mathrm{b}} \overline{N}}{8\pi^2 \omega}. \tag{4}$$

Here, $\gamma = 50$ is a scaling factor, N_{b} is the buoyancy frequency evaluated at the seabed, $\overline{N}$ is the vertical average of the buoyancy frequency, and ω is the frequency of the tidal constituent under evaluation. Values of both N_{b} and $\overline{N}$ follow from the prescription of horizontally uniform stratification $N(z) = N_0 \exp(-z/1300)$, where $N_0 = 5.24 \times 10^{-3}\,\mathrm{s}^{-1}$ has been obtained from a least-squares fit to present-day climatological hydrography (Zaron and Egbert, 2006).

The model solves Eqs. (1)–(2) using forcing from the astronomical tide-generating potential only (represented by ζ_{EQ} in Eq. 1), with the SAL term being derived from TPXO8 (Egbert and Erofeeva, 2002, updated version). An initial spin-up from rest over 7 days is followed by a further 15 days of simulation time, on which harmonic analysis is performed to obtain the tidal elevations and transport. Here, we investigate the two dominating semi-diurnal and diurnal tidal constituents, M_2 and K_1, respectively. The model bathymetry

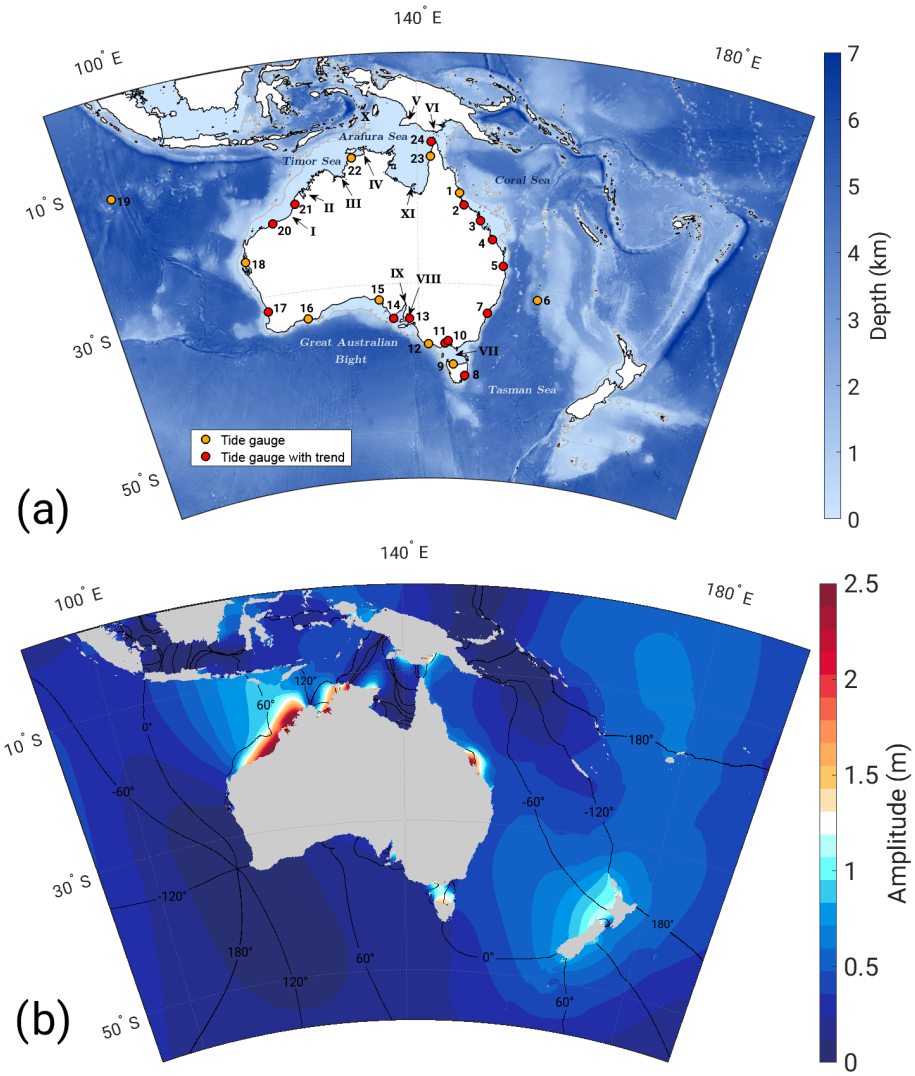

Figure 1. (a) Bathymetry of the model domain and tide gauge sites used in the analysis (coloured dots): see Table 1. Locations at which M_2 trends were estimated are shown in red. Regions mentioned in subsequent sections of the paper are marked on the map: I – Eighty Mile Beach, II – King Sound, III – Joseph Bonaparte Gulf, IV – Van Diemen Gulf, V – Yos Sudarso Island, VI – Torres Strait, VII – Bass Strait, VIII – Gulf St. Vincent, IX – Spencer Gulf, X – Arafura Islands, XI – Wellesley Islands. **(b)** Co-tidal chart of the M_2 constituent amplitude for the control simulation. Black lines represent co-phase lines with 60° separation.

comes from the ETOPO1 dataset (Amante and Eakins, 2009, see Fig. 1 for the present domain), which was averaged to 1/20° horizontal resolution. For the control run with present-day water depths, the domain model heights at the open boundaries were constrained to elevation data from a coarser-resolution global OTIS run, taken from Wilmes et al. (2017). TPXO8 was used to validate the model (alongside tide gauge data at 24 locations); see Sect. 2.4.

2.2 Dissipation computations

The computation of tidal dissipation rates, D, was done following Egbert and Ray (2001):

$$D = W - \nabla \cdot P. \tag{5}$$

Here, W is the work done by the tide-generating force and P is the energy flux given by

$$W = g\rho\langle \mathbf{U} \cdot \nabla(\eta_{\mathrm{SAL}} + \eta_{\mathrm{EQ}})\rangle \tag{6}$$

$$P = g\langle \eta \mathbf{U}\rangle, \tag{7}$$

where the angular brackets mark time averages over a tidal period.

2.3 Implementing sea-level rise

The model runs are split into two sets. In the first, we allow low-lying grid cells to flood as sea level rises, whereas in the second set we introduce vertical walls at the present-day coastline. Following Pelling et al. (2013), we denote

Table 1. Start and end dates of the analysed tide gauge records, including names and running index for identification in Fig. 1.

Station ID	Name	Time span	Source
1	Mourilyan Harbour	1986–2014	GESLA
2	Townsville	1980–2014	GESLA
3	Hay Point	1985–2014	UHSLC
4	Gladstone	1982–2014	UHSLC
5	Brisbane	1985–2016	GESLA
6	Lord Howe Island	1992–2014	GESLA
7	Fort Denison	1965–2017	GESLA
8	Spring Bay	1986–2017	GESLA
9	Burnie	1985–2014	GESLA
10	Williamstown	1976–2014	UHSLC
11	Geelong	1976–2014	UHSLC
12	Portland	1982–2014	GESLA
13	Port Adelaide	1976–2014	GESLA
14	Port Lincoln	1967–2014	UHSLC
15	Thevenard	1966–2014	GESLA
16	Esperance	1985–2017	GESLA
17	Fremantle	1970–2014	GESLA
18	Carnarvon	1991–2014	GESLA
19	Cocos Islands	1991–2017	GESLA
20	Port Hedland	1985–2014	UHSLC
21	Broome	1989–2017	UHSLC
22	Darwin	1991–2017	GESLA
23	Weipa	1986–2014	GESLA
24	Booby Island	1990–2017	UHSLC

these sets "flood" (FL) and "no flood" (NFL), respectively. A range of SLR scenarios corresponding to predicted global mean sea-level increases from large-scale ice sheet collapses (Wilmes et al., 2017) are investigated in both sets. This is done via the implementation of a uniform depth increase across the entire domain of 1, 3, 5, 7, and 12 m. Boundary conditions for each of the SLR scenarios are generated from global simulations. The 5, 7, and 12 m SLR NFL runs were taken directly from Wilmes et al. (2017) and the remaining global simulations were carried out following the methodology outlined in Wilmes et al. (2017) but with varying global sea-level changes and allowing for inundation in the FL runs. Additionally, we simulated tidal responses to future changes in water depth extrapolated from geocentric sea-level trend patterns as observed by satellite altimetry (see Carless et al., 2016; Schindelegger et al., 2018). While such projections contain not only the actual long-term trend of sea level but also significant (sub-)decadal variability, little difference was found for tidal perturbations with respect to our uniform SLR scenarios (see the Supplement). It is also unknown how the magnitude and spatial variation of the trend pattern may change over the period of time required to equate a uniform SLR, especially with the larger scenarios considered here. Hence, in the following, the focus is on the uniform SLR scenarios. We choose to show results for the 1 and 7 m SLR simulations because they best exemplify the changes to tidal characteristics across the domain and also correspond to a high but probable level for the end of this century and an extreme case in which large levels of ice sheet collapse has occurred, respectively (e.g. Wilmes et al., 2017). The simulations with 12 m of SLR have little physical justification, but they allow us to assess how any tidal trends seen up to 7 m, if they appear, may evolve for even higher levels of SLR.

2.4 Model validation

For validation of our numerical experiments, time series of hourly sea-level data from 24 stations around Australasia were obtained from the Global Extreme Sea Level Analysis version 2 (GESLA-2; Woodworth et al., 2017) and the University of Hawaii Sea Level Center (UHSLC; Caldwell et al., 2015); see Table 1. With few exceptions, record lengths are short, but all time series span at least 28 years to allow for an appropriate representation of the 18.61-year nodal cycle in lunar tidal constituents (Haigh et al., 2011). Upon removal of years missing more than 25 % of hourly observations, a three-tiered least-squares fitting procedure was applied to (i) extract mean M_2 and K_1 tidal constants of amplitude H and phase lag G, (ii) deduce linear trends in H and G for both constituents over the complete time series at each station, and (iii) estimate the corresponding long-term trend in MSL. A total of 10 out of 24 tide gauge stations yielded statistically insignificant M_2 amplitude trends at the 95 % confidence level and were thus excluded from the model trend validation below; see Fig. 1 for a graphical illustration.

The processing protocol, essentially taken from Schindelegger et al. (2018), is based on a separation of tidal and non-tidal residuals from the longer-term MSL component through application of a 4-day moving average with Gaussian weighting. The high-frequency filter residuals obtained were then harmonically analysed for 68 tidal constituents using the Matlab® UTide software package (Codiga, 2011), with analysis windows either set to the entire time series (step i) or shifted on an annual basis (step ii). In both cases, we configured UTide for standard least-squares and a white-noise approach in the computation of confidence intervals. Subsequent regressions of annual M_2 tidal constants were performed with a functional model composed of a linear trend, a lag 1-year autocorrelation, AR(1), and sinusoids to account for nodal modulations. Trends in MSL were likewise determined through regression under AR(1) assumptions, upon a priori reduction of the influence of the 18.61-year equilibrium tide.

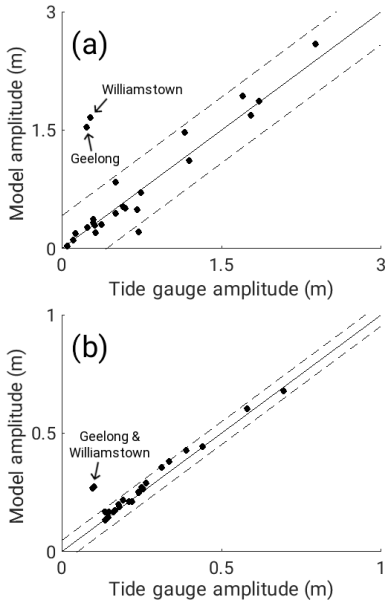

Figure 2. The constituent amplitude at each tide gauge position calculated from GESLA and UHSLC data and the model control simulation for **(a)** M_2 and **(b)** K_1. The solid line marks the zero difference line. The dashed lines mark 1 standard deviation of the difference.

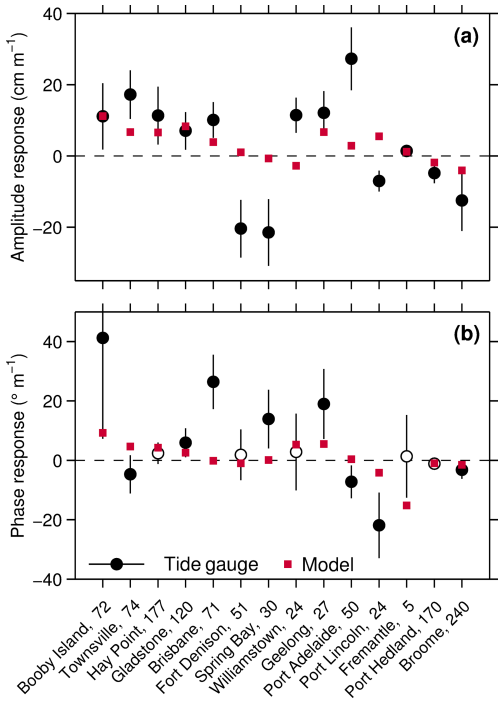

Figure 3. Observed and modelled M_2 response coefficients in **(a)** amplitude H and **(b)** phase lag G per metre of SLR. Model values (red squares) are based on the 1 m FL simulations, while tide gauge estimates at 14 out of 24 locations are shown in black. Error bars correspond to 2 standard deviations, propagated from the trend analyses of sea-level and annual tidal estimates of M_2. Stations with insignificant phase trends (at the 95 % confidence level) are shown as white markers in panel **(b)**. Numbers at the end of the station labelling indicate mean observed M_2 amplitudes (cm).

A regression of the constituent amplitudes calculated from the OTIS control simulation for the present-day bathymetry against the M_2 and K_1 amplitudes from harmonic analysis of the tide gauge data (Fig. 2) reveals that the model performs well at all sample sites except at stations Williamstown and Geelong (see Fig. 1 and Table 1). Here, simulated amplitudes are overestimated by a factor of 5 (M_2) and 2 (K_1), respectively. Both of stations lie on the coast of Port Phillip Bay, a shallow bay isolated from the Bass Strait by two peninsulas. The eastern peninsula is long and narrow, and not resolved in the model bathymetry due to the spatial averaging performed on the source ETOPO1 dataset. As such, the tidal wave from the Bass Strait penetrates into the bay and builds up in amplitude through reflection at lateral boundaries. Excluding Williamstown and Geelong from the comparison, we obtain a root mean square (rms) error for the constituent amplitudes of 17 cm for M_2 and 2 cm for K_1, while correlation coefficients are at 0.97 and 0.99, respectively. Estimates of the median absolute difference between model and test stations can be used to quantify possible biases in a robust way (Stammer et al., 2014); corresponding values are 8 cm for M_2 and 1 cm for K_1 irrespective of whether stations in Port Phillip Bay are included or not. Median phase differences with respect to the tide gauge estimates are 21° for M_2 and 3° for K_1. These statistics give confidence in the model's accuracy and in the assertion that areas where the disagreement between model and tide gauge data is largest are where the resolution of the model has not resolved fine-structure coastal features.

Additional comparisons with gridded M_2 data were performed using the TPXO8 inverse solution, linearly interpolated to the grid of the model domain (see http://volkov.oce.orst.edu/tides, last access: 17 April 2018, for details). The rms difference between the model and the TPXO8 data is 7 cm for M_2 and 2 cm for K_1. The variance capture (VC) of the control was also calculated to see how well the overall character of the tidal constituents was represented (e.g. Pelling and Green, 2013):

$$\mathrm{VC} = 100\left[1 - \left(\frac{\mathrm{RMSD}}{S}\right)^2\right], \tag{8}$$

where RMSD is the rms difference between the control simulation and TPXO8, and S denotes the rms standard deviation of the TPXO8 amplitudes. The VC is above 96 % for M_2 and 97 % for K_1.

For validation of the simulated M_2 changes under SLR, we followed Schindelegger et al. (2018) and condensed measured M_2 trends (∂H, ∂G) and MSL rates (∂s) to response coefficients in amplitude ($r_H = \partial H/\partial s$) and phase ($r_G = \partial G/\partial s$). Simulated amplitude and phase changes from the

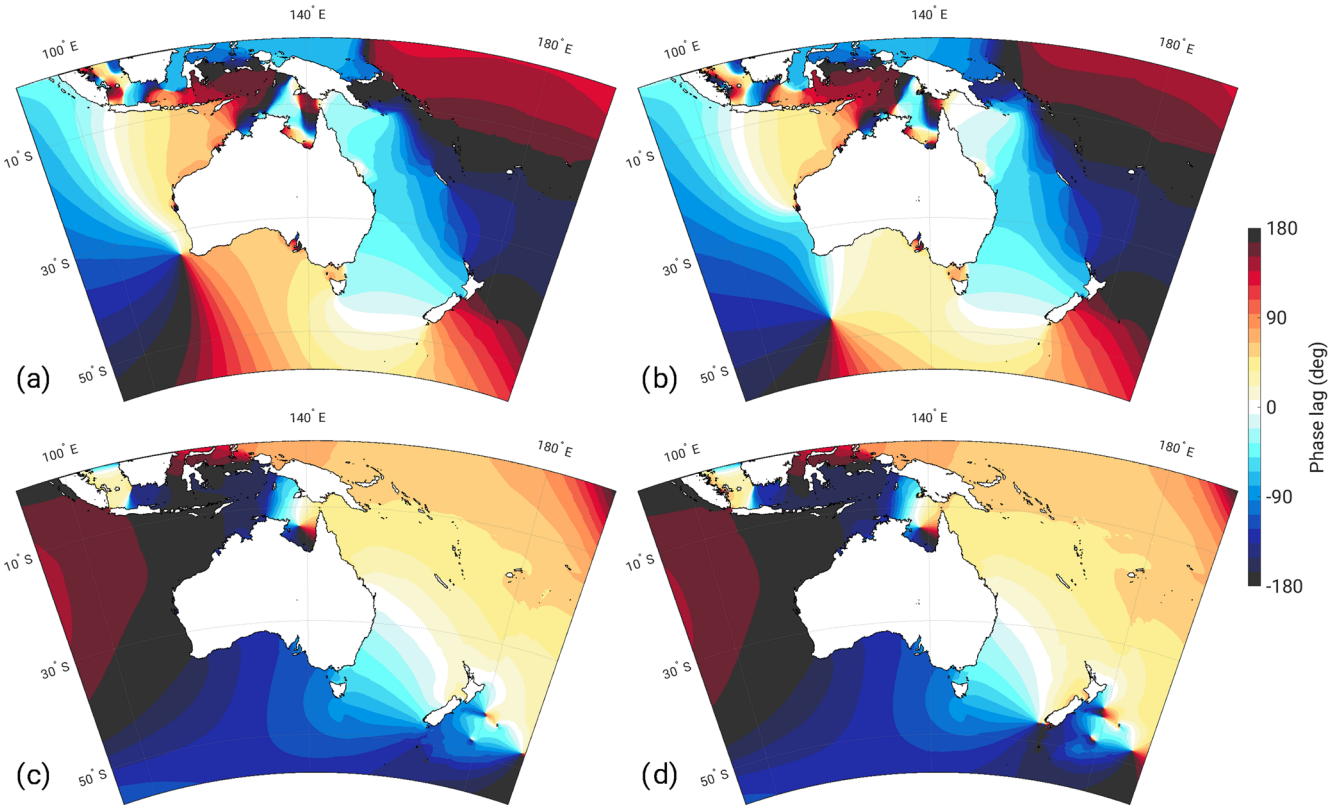

Figure 4. The constituent phase lags with respect to the Greenwich meridian (°) for the control **(a, c)** and 7 m SLR **(b, d)** simulations for M_2 **(a, b)** and K_1 **(c, d)**.

1 m FL run at the location of 14 tide gauges were interpolated from nearest-neighbour cells and also converted to ratios of r_H and r_G. Graphical comparisons in Fig. 3 indicate that the model captures the sign of the observed M_2 amplitude response in 10 out of 14 cases and reproduces large fractions of the in situ variability at approximately half of the analysed stations (e.g. Booby Island, Brisbane, Geelong, Port Hedland, Broome). A similar figure for K_1 can be found in the supporting information. Model-to-data disparities on the northeastern seaboard (Hay Point, Gladstone) are markedly reduced in comparison to Schindelegger et al. (2018, their Fig. 7) due to the higher horizontal resolution of our setup in a region of ragged coastline features. Neither the increase of M_2 amplitudes at Townsville nor the pronounced reduction of the tide at Fort Denison (Sydney Harbour) can be explained by SLR perturbations in the tidal model; both signals may be the effect of periodic dredging to maintain acceptable water depths for port operations; see Devlin et al. (2014) for a similar analysis. The decrease of the small M_2 tide at Spring Bay, Tasmania (20 cm m^{-1} of SLR), remains puzzling though, given that the gauge is open to the sea and unaffected by harbour activities or variable river discharge rates. Mechanisms other than SLR, such as modulation of the internal tide due to stratification changes along its path of propagation (Colosi and Munk, 2006) or variations in barotropic transport induced by thermocline deepening (Müller, 2012), need to be thoroughly addressed to complete the picture of secular changes in the surface tide. Furthermore, uncertainty in the bathymetric data due to sparsity of sounding observations may induce additional errors. Despite these limitations, our 1 m FL simulation captures good portions of the patterns of M_2 amplitude changes seen in tide gauge records around Australasia. Moreover, on timescales of centuries, water column depth changes due to SLR will outweigh tidal perturbations from other physical mechanisms. Hence, we conclude that our simulations lend themselves well for analysis of probable future tidal changes over a wider area.

3 Results

The control run exemplifies the typical tidal environment of the model domain (Figs. 1b and 4a). M_2 has large amplitudes along the north-west coast of Australia and within Joseph Bonaparte Gulf and Van Diemen Gulf. To the south-west of Australia lies a clockwise-rotating amphidrome, responsible for the westward propagation of the tidal wave across the north Australian Shelf. The interaction of this wave with the confined topography of the Arafura Sea leads to a complex tidal pattern with a notable amphidrome north of the Gulf

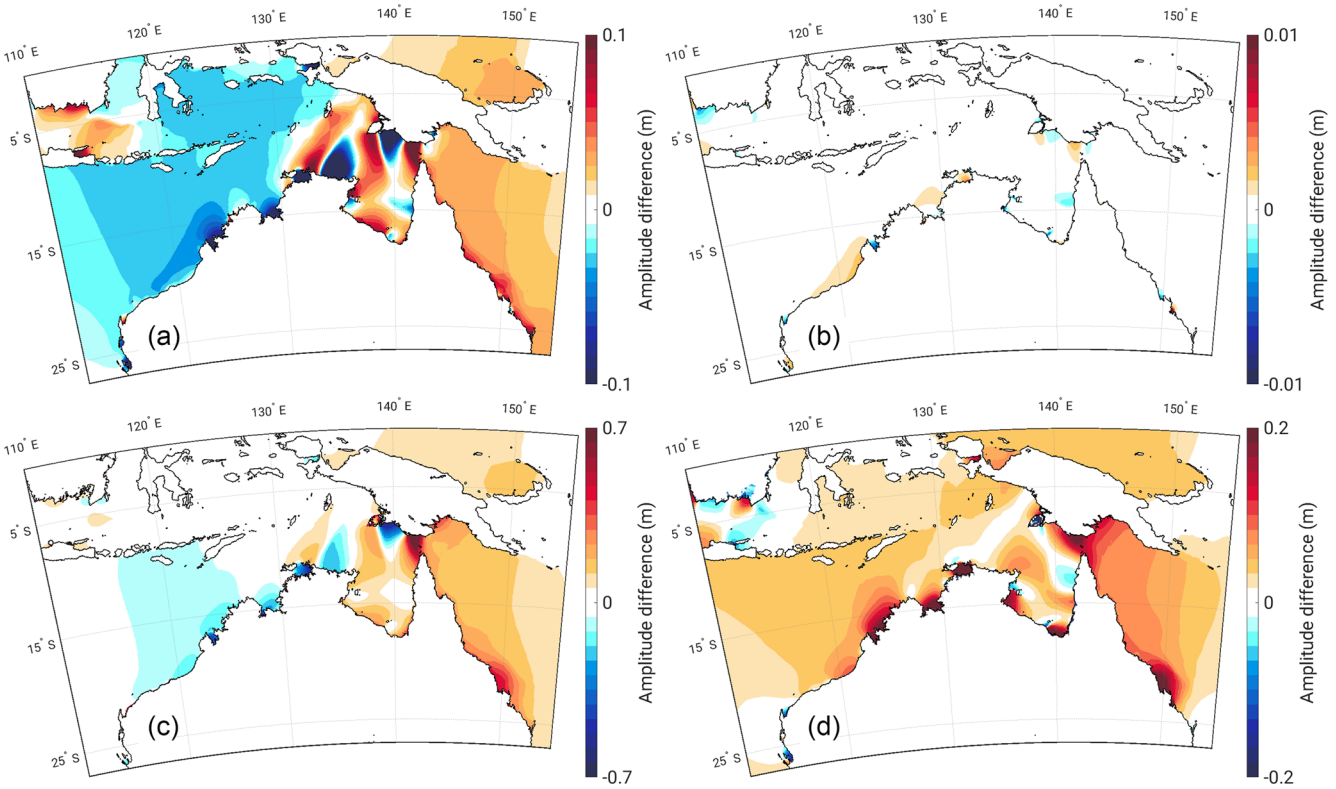

Figure 5. The difference in M_2 amplitude (m) between the FL and control simulation (i.e. FL–control) for 1 m SLR **(a)** and 7 m SLR **(c)** alongside the difference between the NFL and FL simulations (i.e. NFL–FL) for 1 m SLR **(b)** and 7 m SLR **(d)**. The scale applied to panels **(a)** and **(c)** is relative to the applied SLR scenario. Regions that appear blue in panels **(b)** and **(d)** are where the FL amplitude is greater than the NFL amplitude; as such, coastal areas which have been flooded will appear blue.

of Carpentaria. The tide rotates anti-clockwise around New Zealand towards the east coast of Australia, where large amplitudes can be seen between Hay Point and Gladstone. K_1 is dominated by a single amphidrome located within the Gulf of Carpentaria, with raised amplitudes to the north and south of this point (see the Supplement).

In general, for both constituents, the amplitude changes are not linear with respect to the imposed level of SLR (see Idier et al., 2017; Pickering et al., 2017, where tidal amplitudes across the European Shelf changed non-proportionally with SLR greater than 2 m). Relative changes are larger for lower SLR scenarios (e.g. 1 m) than for the higher SLR scenarios (e.g. 7 m). No significant differences between the FL and NFL scenarios for 1 m SLR can be seen, likely due to the fact that allowing land to flood at a 1 m SLR scenario only increased the wetted area by 12 grid cells (on our 1166×2000 computational grid), while at 7 m SLR 3320 new ocean grid cells were generated. Accordingly, for larger sea-level increases, the differences between the Fl and NFL scenarios become more pronounced due to the increased number of flooded cells. A detailed analysis of the impact of SLR on M_2, and more peripherally K_1, is given below; the most common locations discussed are shown in Fig. 1a.

3.1 Effect of SLR on the M_2 tide

SLR brings some fairly significant changes to the M_2 tidal systems around Australia. Many of the regions which stand out as having high M_2 amplitude at present (see Fig. 1b) suffer a marked reduction in amplitude with increasing SLR (Fig. 5a and c). To the north-west of Australia, amplitudes decrease in regions centred around King Sound, around Joseph Bonaparte Gulf, within Van Diemen Gulf, and across the Timor Sea. The reduction in amplitude to the north-east of Van Diemen Gulf comes alongside the formation of a new amphidrome; the phase lines that run north-south in the Arafura Sea (Fig. 1b) move closer together before coalescing to form an amphidromic point. A further amphidromic point emerges in the south-east of the Gulf of Carpentaria, around the Wellesley Islands, when a virtual amphidromic point (an amphidrome over land) moves north to become real (an amphidrome over the ocean). Both these points form some time between 3 and 5 m SLR (not shown). The amphidrome that sits north of the Gulf of Carpentaria (Fig. 4a) moves northwards with SLR in both the FL and NFL scenarios, eventually becoming virtual at the higher SLR scenarios by moving over Yos Sudarso Island. This movement is therefore associated with the change in the propagation properties of the

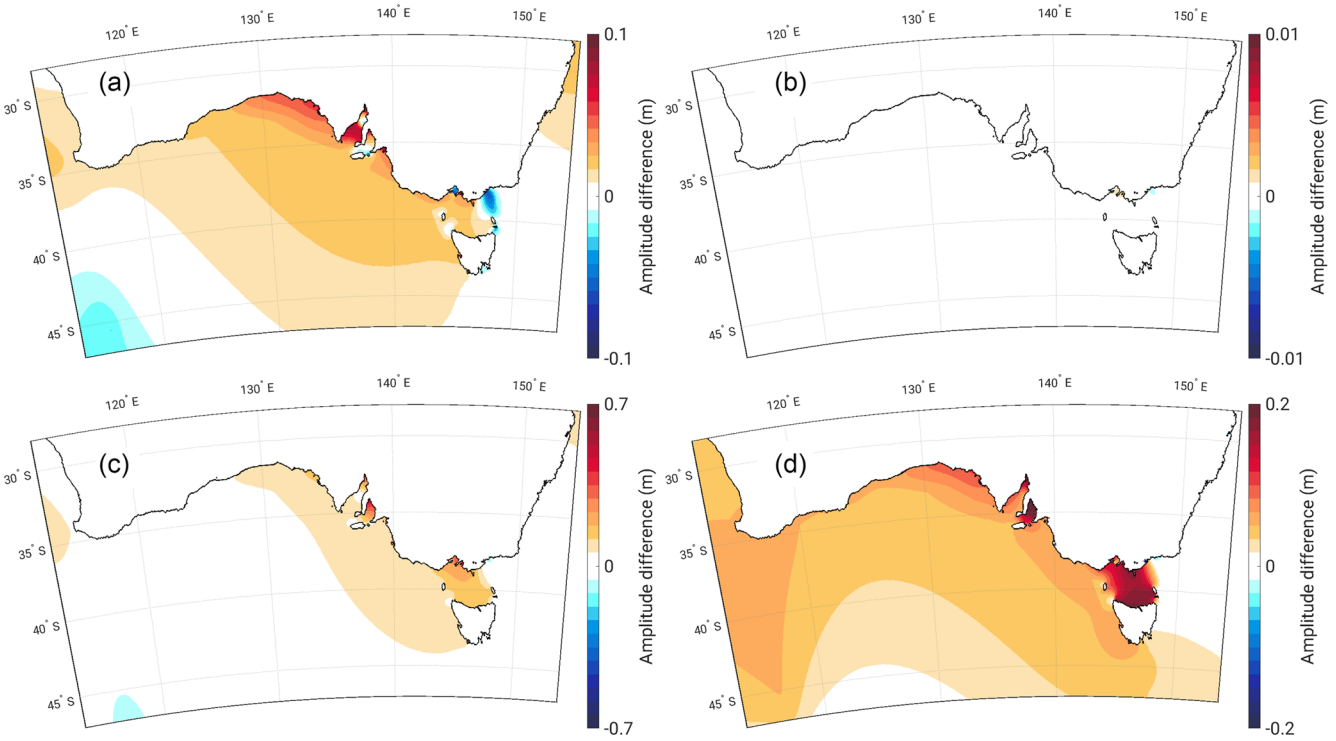

Figure 6. Same as Fig. 5 but showing the south coast of Australia.

incoming tidal wave, rather than the inundation of Yos Sudarso Island which occurs at 5 m SLR and above.

The Torres Strait features a sharp divide between a large positive and small or weakly negative amplitude difference on its west and east sides, respectively. The strait is shallow and dotted with islands, restricting the flow of the tides. Absolute amplitudes on the east side are initially elevated compared to the west (Fig. 1b) but this difference is mitigated with increasing SLR, as the larger volume of the channel allows for enhanced tidal transport across the strait (Fig. 5a and c).

In the remaining part of the domain, the M_2 amplitudes around the coast of New Zealand and along the east coast of Australia, particularly between Hay Point and Gladstone (Fig. 1a, points 3 and 4), both increase with SLR. In the Bass Strait, shown in Fig. 6, the amplitude also increases along with SLR; however, there is a slight drop in amplitude at 1 m SLR at the eastern entrance of the strait and within Port Phillip Bay (the location of the Geelong and Williamstown tide gauges). These decreases quickly disappear at higher SLR. Along the south coast of Australia, the amplitudes also increase with SLR, but the simulated perturbations there are generally smaller in magnitude than in the north (see also Schindelegger et al., 2018). Increased tidal amplitudes at the head and mouth of Spencer Gulf (Fig. 6a) are associated with a slight weakening of a standing-wave-like pattern where M_2 amplitudes increase from the sea towards inland (Fig. 1b). However, this feature does not evolve proportionally with the imposed level of SLR (see Fig. 6c for the 7 m case). To the east, in Gulf St. Vincent, there is a similar, if stronger, standing-wave-like pattern (Fig. 1b). Here, the elevated amplitudes proximity to the coast increase in line with SLR (Fig. 6c). Moving further west along the south coast of Australia, the amphidromic point off the south-west coast moves southwards with increasing SLR (Fig. 4a and b), with a faster progression in the NFL than in the FL runs. Note that, almost universally across the domain, the amplitudes seen in the NFL runs are higher than those in the FL runs (Figs. 5d and 6d). It is clear that allowing flooding to occur suppresses the magnitude of any SLR effect upon tidal amplitude.

Additionally, we have repeated our control and future simulations using boundary conditions taken from TPXO8, i.e. using present-day boundary conditions, instead of those from global SLR simulations. In these runs, the magnitude and spatial distribution of the amplitude changes are vastly different from the results presented above. Figure 7 demonstrates, and allows for a comparison of, the pattern of amplitude changes seen for M_2 north of Australia in these runs. Especially striking is the difference in magnitude of tidal amplitude increases along the east coast of Australia. Applying present-day boundary conditions leads to a very strong underestimation of the amplitude changes in this area (the differences exceed 40 cm in some locations). Similarly pronounced is the difference on the north-west coast where the run with present-day boundary conditions overestimates the amplitude decreases. In large parts of the Arafura Sea, the

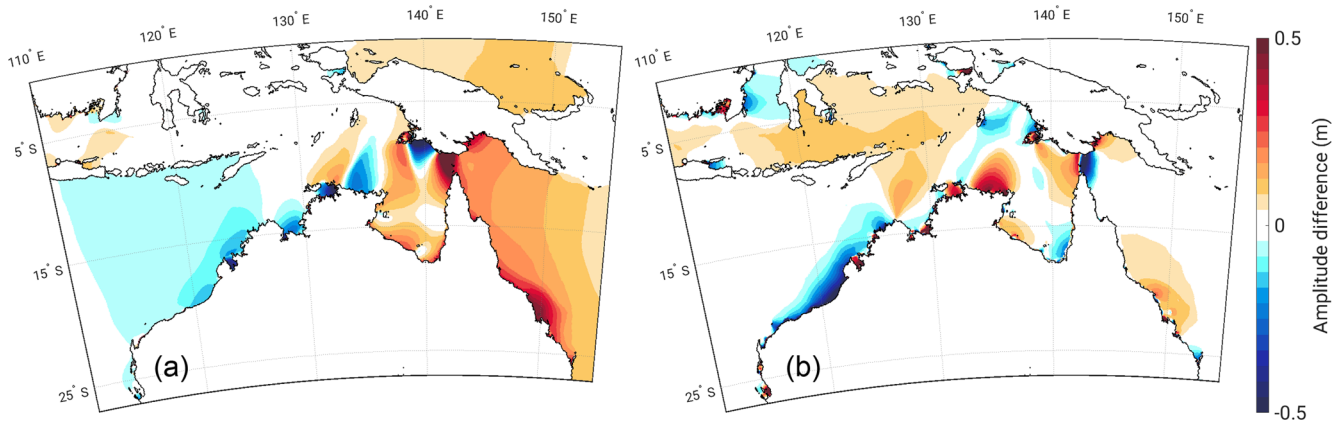

Figure 7. The difference in M_2 amplitude (m) between the FL and control simulation (i.e. FL–control) for 7 m SLR using boundary conditions generated from a global 7 m SLR scenario **(a)** and using boundary conditions generated from TPXO8 **(b)**.

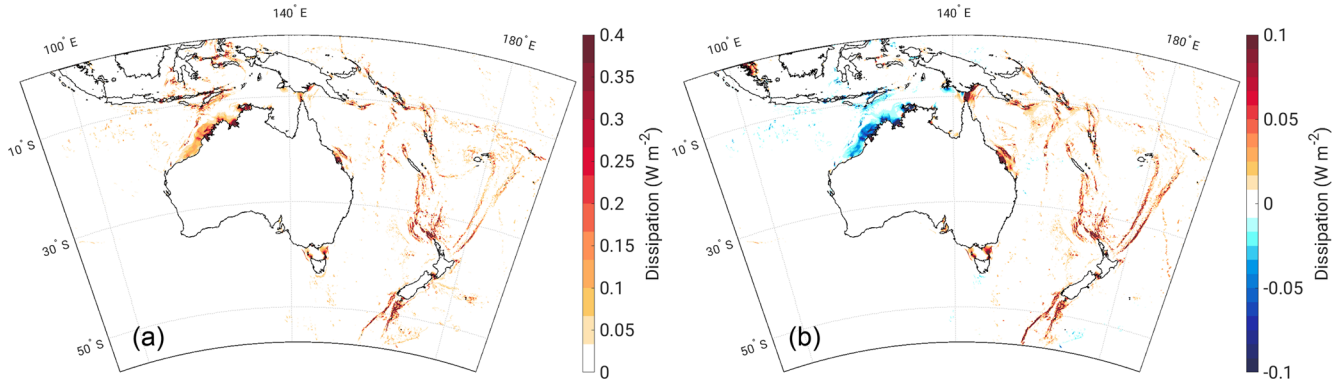

Figure 8. The dissipation (W m^{-2}) associated with the M_2 constituent across the entire model domain **(a)** and the difference in dissipation between the 7 m FL simulation and the control run (i.e. FL–control, **b**).

tidal amplitude responses are of opposite sign in response to the different boundary conditions. This is a key result and it highlights the importance of applying correct boundary conditions for regional simulations which take into account the far-field change occurring outside the model domain.

Figure 8a displays the dissipation associated with the M_2 tidal constituent for the control simulation. It is evident that a majority of the energy is lost at the coast and on the shelf, especially around sharp and shallow bathymetric features. There is a remarkable reduction in dissipation along the north-west coast of Australia with SLR, matching areas with a marked decrease in tidal amplitude (Fig. 8b). There are small pockets of dissipation increases in proximity to the coast in the north-west, associated with areas of enhanced flooding. Much of the dissipation increases within the domain come from the undersea ridges and trenches to the north and south of New Zealand, as well as the east side of the Torres Strait, the area between Hay Point and Gladstone on the east coast of Australia (at the southern extent of the Great Barrier Reef), and both ends of the Bass Strait. All of these

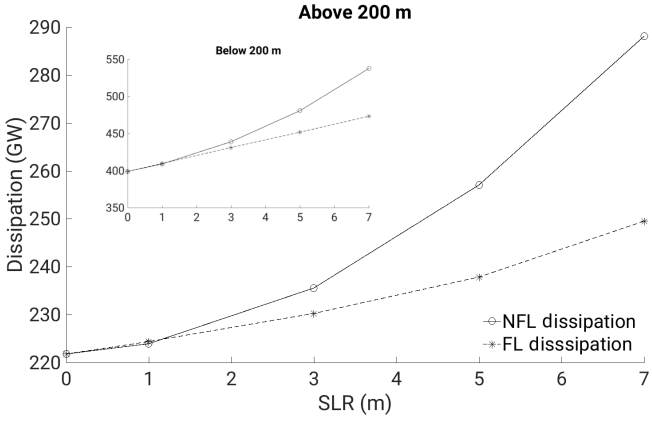

Figure 9. The dissipation totals (GW) across the model domain above and below (inset) the depth of the 200 m isobath of the control bathymetry.

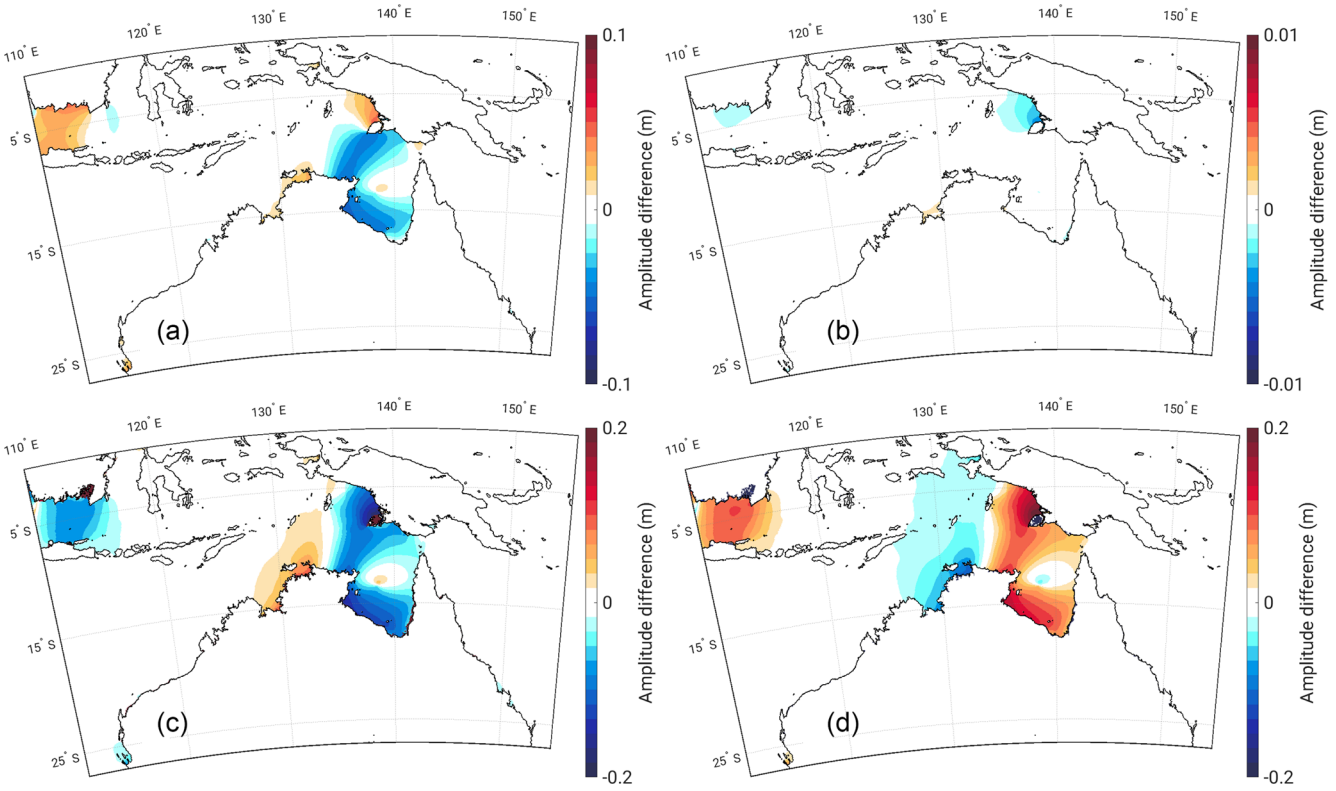

Figure 10. Same as Fig. 5 but for the K_1 constituent.

areas are associated with an increase in M_2 amplitude with SLR.

The impact upon the total dissipation across the domain by allowing flooding is illustrated in Fig. 9. In both the NFL and FL runs, dissipation increases with SLR; the dissipation generated by areas with increased amplitudes outweighs the loss of dissipation in areas of decreased amplitude. With amplitudes in the NFL runs being much higher than in the FL runs, the corresponding dissipation is higher, and the gap in dissipation between the NFL and FL simulations widens with increasing SLR. At 12 m SLR, the NFL dissipation begins to plateau, whilst the FL dissipation continues to rise. Overall, dissipation on the shelf (nominally above the 200 m isobath, accounting for approximately 7 % of the water-covered area of the domain) amounts to about half of the energy dissipated in deeper water.

3.2 Effect of SLR on the K_1 tide

The changes to K_1 are relatively small in comparison to the changes seen for the semi-diurnal constituent. The main point of interest is the amphidromic system in the Gulf of Carpentaria. Figure 10 shows an initial negative amplitude response in the north and south of the Gulf, while there are slight increases in amplitude north of Yos Sudarso Island and in the Java Sea. The position of the amphidromic system is relatively stable with SLR, as evident from the constituent phase plots in Fig. 4c and d, and it is evident that K_1 suffers a decrease in amplitude around the Gulf of Carpentaria with SLR. Comparing Fig. 10c and d, a majority of the amplitude difference occurring in the FL scenario is negated when impermeable coastlines are implemented. The dissipation for which K_1 is responsible in the domain is approximately 7 times smaller than that of M_2 and therefore not discussed further.

3.3 Synthesis

One of the most striking characteristics of the response of the semi-diurnal constituents to SLR is the drop in amplitude along the north-west coast of Australia, an area where a large amount of dissipation occurs in the control. We associate this feature with the altered propagation properties of the incoming tidal wave, as the imposed sea-level change in our simulations represents a significant fraction of the average water depth across the shelf; for instance, the 7 m SLR scenario increases the depth of the Gulf of Carpentaria by $\sim 10\,\%$. As the tidal system goes from hosting a single wave propagating across the Arafura Sea to something more complex with multiple amphidromes within the basin, the semi-diurnal resonant response on the shelf is interrupted. This dynamical change may explain the drop in amplitudes to the north-west of Australia.

4 Discussion

It has been shown here, using a validated tidal model, that the tidal characteristics around Australia are sensitive to water column depth changes due to SLR. We show significant changes in tidal amplitudes due to the SLR, with the largest change in amplitude being 15 % of the SLR signal south of Papua New Guinea and north-east of Van Diemen Gulf. The model can reproduce considerable fractions of the tidal amplitude change signals seen in the tide gauge record. This is a strong indication that the observed changes in tides are, at least in part, driven by sea-level changes, and adds further motivation for our investigation.

Somewhat surprisingly, the responses of the tides to SLR are very different in both their sign and spatial patterns depending on how the open boundary conditions are implemented. Furthermore, in the simulations with TPXO8 data on the open boundary, the amplitude changes along the north-east coast, home to several population centres, are strongly underestimated. The take-home message here is that, opposite to what has often been assumed (e.g. Pelling and Green, 2013), simulations of the effect of SLR on tides for certain regions should not use present-day boundary conditions, even if the open boundary is in the far field. There are also pronounced differences between the FL and NFL simulations. Consequently, to make accurate predictions of the future tides, local coastal defence strategies need to be known, because allowing land to flood could mitigate increases in the tidal range induced by the rising sea level. If this information is not obtainable, both scenarios need to be investigated.

However, this introduces another problem: most of Australia's largest cities lie on or near the coast, and many of them are close to the areas which may experience the largest tidal changes with SLR. It thus opens for an interesting investigation to see if unpopulated areas of the coastline could be flooded to mitigate the rising sea level in a hybrid NFL–FL scenario. Adopting a more dynamical perspective, numerical tests employing wave forcing of different periods are proposed to distinguish if the tidal response of certain areas within the domain is largely due to resonance or frictional effects (Idier et al., 2017). Additionally, an investigation into the coupling of tidal changes for expected magnitudes of SLR and storm surges (Muis et al., 2016) within the domain could provide further insight and guidance to the future planning of coastal defences around Australia.

In conclusion, the series of simulations presented here have shown that the tidal amplitudes along the northern coast of Australia and around the Sahul Shelf region are particularly sensitive to SLR. Coastal population centres such as Adelaide and Mackay are predicted to have to deal with the consequences of increased tidal amplitudes with increasing SLR. SLR appears to be moving the semi-diurnal constituents away from resonance on the shelf and only have a small impact on the diurnal constituents in the Gulf of Carpentaria. The implementation of flooding can have a significant impact on the response of the tide by locally increasing dissipation and should be considered essential for future tidal modelling with SLR.

Data availability. The sea-level data came from UHSLC (https://doi.org/10.7289/V5V40S7W, Caldwell et al., 2015) and GESLA-2 (https://doi.org/10.5285/3b602f74-8374-1e90-e053-6c86abc08d39, Woodworth et al., 2017). Model results are available from the authors upon request.

Supplement. The supplement related to this article is available online at: https://doi.org/10.5194/os-15-147-2019-supplement.

Author contributions. The experiments were originally carried out by AH as a student under the supervision of JAMG. JAMG performed further regional model runs utilising data from SBW's global simulations. MS performed the model validation. AH prepared the manuscript with contributions from all co-authors.

Competing interests. The authors declare that they have no conflict of interest.

Special issue statement. This article is part of the special issue "Developments in the science and history of tides (OS/ACP/HGSS/NPG/SE inter-journal SI)". It is not associated with a conference.

Acknowledgements. Financial support for this study was made available by the UK Natural Environmental Research Council (grant NE/I030224/1, awarded to J. A. Mattias Green) and the Austrian Science Fund (FWF, through project P30097-N29 awarded to Michael Schindelegger). All numerical simulations were performed using HPC Wales' supercomputer facilities.

Edited by: Philip Woodworth
Reviewed by: two anonymous referees

References

ABS: Australia (AUST) 2011/2016 Census QuickStats, Australian Bureau of Statistics (ABS), available at: http://quickstats.censusdata.abs.gov.au/census_services/getproduct/census/2016/quickstat/036?opendocument (last access: 9 November 2018), 2016.

Allen, G. P., Salomon, J. C., Bassoullet, P., Penhoat, Y. D., and de Grandpré, C.: Effects of tides on mixing and suspended sediment transport in macrotidal estuaries, Sediment. Geol., 26, 69–90, https://doi.org/10.1016/0037-0738(80)90006-8, 1980.

Amante, C. and Eakins, B. W.: ETOPO1 1 arcmin Global Relief Model: Procedures, Data Sources and Analysis, NOAA Tech-

nical Memorandum NESDIS NGDC-24, National Geophysical Data Center, NOAA, https://doi.org/10.7289/V5C8276M, 2009.

Caldwell, P. C., Merrifield, M. A., and Thompson, P. R.: Sea level measured by tide gauges from global oceans – the Joint Archive for Sea Level holdings (NCEI Accession 0019568), NOAA National Centers for Environmental Information, Version 5.5, Dataset, https://doi.org/10.7289/V5V40S7W, 2015.

Carless, S., Green, J., Pelling, H., and Wilmes, S.-B.: Effects of future sea-level rise on tidal processes on the Patagonian Shelf, J. Marine Syst., 163, 113–124, https://doi.org/10.1016/j.jmarsys.2016.07.007, 2016.

Cazenave, A. and Llovel, W.: Contemporary Sea Level Rise, Ann. Rev. Mar. Sci., 2, 145–173, https://doi.org/10.1146/annurev-marine-120308-081105, 2010.

Church, J. A. and White, N. J.: Sea-Level Rise from the Late 19th to the Early 21st Century, Surv. Geophys., 32, 585–602, https://doi.org/10.1007/s10712-011-9119-1, 2011.

Church, J. A., Monselesan, D., Gregory, J. M., and Marzeion, B.: Evaluating the ability of process based models to project sea-level change, Environ. Res. Lett., 8, 014051, https://doi.org/10.1088/1748-9326/8/1/014051, 2013.

Codiga, D. L.: Unified tidal analysis and prediction using the UTide Matlab functions, Graduate School of Oceanography, University of Rhode Island Narragansett, RI, 2011.

Colosi, J. A. and Munk, W.: Tales of the venerable Honolulu tide gauge, J. Phys. Oceanogr., 36, 967–996, https://doi.org/10.1175/JPO2876.1, 2006.

Dangendorf, S., Marcos, M., Wöppelmann, G., Conrad, C. P., Frederikse, T., and Riva, R.: Reassessment of 20th century global mean sea level rise, P. Natl. Acad. Sci. USA, 114, 5946–5951, https://doi.org/10.1073/pnas.1616007114, 2017.

DeConto, R. M. and Pollard, D.: Contribution of Antarctica to past and future sea-level rise, Nature, 531, 591–597, https://doi.org/10.1038/nature17145, 2016.

Devlin, A. T., Jay, D. A., Talke, S. A., and Zaron, E.: Can tidal perturbations associated with sea level variations in the western Pacific Ocean be used to understand future effects of tidal evolution?, Ocean Dynam., 64, 1093–1120, https://doi.org/10.1007/s10236-014-0741-6, 2014.

Egbert, G. D. and Erofeeva, S. Y.: Efficient inverse modeling of barotropic ocean tides, J. Atmos. Ocean. Tech., 19, 183–204, https://doi.org/10.1175/JPO2876.1, 2002.

Egbert, G. D. and Ray, R. D.: Estimates of M_2 tidal energy dissipation from Topex/Poseidon altimeter data, J. Geophys. Res.-Oceans, 106, 22475–22502, https://doi.org/10.1029/2000JC000699, 2001.

Egbert, G. D., Bills, B. G., and Ray, R. D.: Numerical modeling of the global semidiurnal tide in the present day and in the last glacial maximum, J. Geophys. Res.-Oceans, 109, C03003, https://doi.org/10.1029/2003JC001973, 2004.

Green, J., Huber, M., Waltham, D., Buzan, J., and Wells, M.: Explicitly modeled deep-time tidal dissipation and its implication for Lunar history, Earth Planet. Sc. Lett., 461, 46–53, https://doi.org/10.1016/j.epsl.2016.12.038, 2017.

Green, J. A. M.: Ocean tides and resonance, Ocean Dynam., 60, 1243–1253, https://doi.org/10.1007/s10236-010-0331-1, 2010.

Green, J. A. M. and Huber, M.: Tidal dissipation in the early Eocene and implications for ocean mixing, Geophys. Res. Lett., 40, 2707–2713, https://doi.org/10.1002/grl.50510, 2013.

Greenberg, D. A., Blanchard, W., Smith, B., and Barrow, E.: Climate change, mean sea level and high tides in the Bay of Fundy, Atmos. Ocean, 50, 261–276, https://doi.org/10.1080/07055900.2012.668670, 2012.

Haigh, I. D., Eliot, M., and Pattiaratchi, C.: Global influences of the 18.61 year nodal cycle and 8.85 year cycle of lunar perigee on high tidal levels, J. Geophys. Res.-Oceans, 116, C06025, https://doi.org/10.1029/2010JC006645, 2011.

Hay, C. C., Morrow, E., Kopp, R. E., and Mitrovica, J. X.: Probabilistic reanalysis of twentieth-century sea-level rise, Nature, 517, 481–484, https://doi.org/10.1038/nature14093, 2015.

Hendershott, M. C.: Numerical models of ocean tides, in: The Sea, vol. 6, 47–89, Wiley Interscience Publication, 1977.

Idier, D., Paris, F., Le Cozannet, G., Boulahya, F., and Dumas, F.: Sea-level rise impacts on the tides of the European Shelf, Cont. Shelf Res., 137, 56–71, https://doi.org/10.1016/j.csr.2017.01.007, 2017.

IPCC: Climate Change 2013: The Physical Science Basis, Contribution of Working Group I to the Fifth Assessment Report of the Intergovernmental Panel on Climate Change, Cambridge University Press, Cambridge, UK, New York, NY, USA, https://doi.org/10.1017/CBO9781107415324, 2013.

McInnes, K. L., Church, J., Monselesan, D., Hunter, J. R., O'Grady, J. G., Haigh, I. D., and Zhang, X.: Information for Australian impact and adaptation planning in response to sea-level rise, Aust. Meteorol. Ocean, 65, 127–149, 2015.

Muis, S., Verlaan, M., Winsemius, H. C., Aerts, J. C. J. H., and Ward, P. J.: A global reanalysis of storm surges and extreme sea levels, Nat. Commun., 7, 11969, https://doi.org/10.1038/ncomms11969, 2016.

Müller, M.: The influence of changing stratification conditions on barotropic tidal transport and its implications for seasonal and secular changes of tides, Cont. Shelf Res., 47, 107–118, https://doi.org/10.1016/j.csr.2012.07.003, 2012.

Müller, M., Arbic, B. K., and Mitrovica, J. X.: Secular trends in ocean tides: Observations and model results, J. Geophys. Res.-Oceans, 116, C05013, https://doi.org/10.1029/2010JC006387, 2011.

Pelling, H. E. and Green, J. A. M.: Sea level rise and tidal power plants in the Gulf of Maine, J. Geophys. Res.-Oceans, 118, 2863–2873, https://doi.org/10.1002/jgrc.20221, 2013.

Pelling, H. E., Green, J. A. M., and Ward, S. L.: Modelling tides and sea-level rise: To flood or not to flood, Ocean Model., 63, 21–29, https://doi.org/10.1016/j.ocemod.2012.12.004, 2013.

Pickering, M., Horsburgh, K. J., Blundell, J. R., Hirschi, J. J.-M., Nicholls, R. J., Verlaan, M., and Wells, N. C.: The impact of future sea-level rise on the global tides, Cont. Shelf Res., 142, 50–68, https://doi.org/10.1016/j.csr.2017.02.004, 2017.

Pugh, D. and Woodworth, P.: Sea-Level Science: Understanding tides, surges, tsunamis and mean sea-level changes, Cambridge University Press, Cambridge, UK, 2014.

Schindelegger, M., Green, J. A. M., Wilmes, S.-B., and Haigh, I. D.: Can we model the effect of observed sea level rise on tides?, J. Geophys. Res.-Oceans, 123, 4593–4609, https://doi.org/10.1029/2018JC013959, 2018.

Slangen, A. B. A., Katsman, C. A., van de Wal, R. S. W., Vermeersen, L. L. A., and Riva, R. E. M.: Towards regional projections of twenty-first century sea-level change based

on IPCC SRES scenarios, Climate Dynam., 38, 1191–1209, https://doi.org/10.1007/s00382-011-1057-6, 2012.

Stammer, D., Ray, R. D., Andersen, O. B., Arbic, B. K., Bosch, W., Carrère, L., Cheng, Y., Chinn, D. S., Dushaw, B. D., Egbert, G. D., Erofeeva, S. Y., Fok, H. S., Green, J. A. M., Griffiths, S., King, M. A., Lapin, V., Lemoine, F. G., Luthcke, S. B., Lyard, F., Morison, J., Müller, M., Padman, L., Richman, J. G., Shriver, J. F., Shum, C. K., Taguchi, E., and Yi, Y.: Accuracy assessment of global barotropic ocean tide models, Rev. Geophys., 52, 243–282, https://doi.org/10.1002/2014RG000450, 2014.

Stumpf, R. P. and Haines, J. W.: Variations in Tidal Level in the Gulf of Mexico and Implications for Tidal Wetlands, Estuar. Coast Shelf S., 46, 165–173, https://doi.org/10.1006/ecss.1997.0276, 1998.

Vellinga, P., Katsman, C., Sterl, A., Beersma, J. J., Hazeleger, W., Church, J., Kopp, R., Kroon, D., Oppenheimer, M., Plag, H. P., Rahmstorf, S., Lowe, J., Ridley, J., von Storch, H., Vaughan, D., van der Wal, R., Weisse, R., Kwadijk, J., Lammersen, R., and Marinova, N. A.: Exploring high-end climate change scenarios for flood protection of the Netherlands, Tech. rep., Royal Netherlands Meteorological Institute, 2009.

Watson, P. J.: Is There Evidence Yet of Acceleration in Mean Sea Level Rise around Mainland Australia?, J. Coastal Res., 27, 369–377, 2011.

Webb, D. J.: On the shelf resonances of the Gulf of Carpentaria and the Arafura Sea, Ocean Sci., 8, 733–750, https://doi.org/10.5194/os-8-733-2012, 2012.

White, N. J., Haigh, I. D., Church, J. A., Koen, T., Watson, C. S., Pritchard, T. R., Watson, P. J., Burgette, R. J., McInnes, K. L., You, Z.-J., Zhang, X., and Tregoning, P.: Australian sea levels–Trends, regional variability and influencing factors, Earth-Sci. Rev., 136, 155–174, https://doi.org/10.1016/j.earscirev.2014.05.011, 2014.

Wilmes, S.-B. and Green, J. A. M.: The evolution of tides and tidally driven mixing over 21,000 years, J. Geophys. Res.-Oceans, 119, 4083–4100, https://doi.org/10.1002/2013JC009605, 2014.

Wilmes, S.-B., Green, J. A. M., Gomez, N., Rippeth, T. P., and Lau, H.: Global tidal impacts of large-scale ice sheet collapses, J. Geophys. Res.-Oceans, 122, 8354–8370, https://doi.org/10.1002/2017JC013109, 2017.

Woodworth, P. L.: A survey of recent changes in the main components of the ocean tide, Cont. Shelf Res., 30, 1680–1691, https://doi.org/10.1016/j.csr.2010.07.002, 2010.

Woodworth, P. L., Hunter, J. R., Marcos, M., Caldwell, P., Menéndez, M., and Haigh, I.: Towards a global higher-frequency sea level dataset, Geosci. Data J., 3, 50–59, https://doi.org/10.1002/gdj3.42, 2017.

Zaron, E. D. and Egbert, G. D.: Estimating open-ocean barotropic tidal dissipation: the Hawaiian ridge, J. Phys. Oceanogr., 36, 1019–1035, https://doi.org/10.1175/JPO2878.1, 2006.

Zhang, X., Church, J. A., Monselesan, D., and McInnes, K. L.: Sea level projections for the Australian region in the 21st century, Geophys. Res. Lett., 44, 8481–8491, https://doi.org/10.1002/2017GL074176, 2017.